Fifth Drag Prediction Workshop: ONERA Investigations with Experimental Wing Twist and Laminarity

David Hue

5th Drag Prediction Workshop: CFD Investigations with Experimental Wing Twist and Laminar Leading Edge

David HUE[1]
ONERA, the French Aerospace Lab, 92190 Meudon, France

This article is aimed at presenting the computational studies which have been performed at ONERA in 2013 in the framework of the 5th AIAA Drag Prediction Workshop (DPW-5). As data concerning the Common Research Model (CRM) configuration was collected from the NASA Langley and Ames wind tunnels, a significant discrepancy appeared between the experimental and computational pitching moment evaluations. Investigations carried out by NASA in 2012 showed that the experimental model and the numerical geometry were slightly different. Indeed, the wing twist measured in the wind tunnels was different from the one that was used for the computational analyses. Therefore, new Computational Fluid Dynamics (CFD) studies using the CRM Wing-Body configuration with the corrected wing twist have been completed at ONERA. The common Multi-Block (MB) grids provided by the DPW-5 Committee have been adequately modified before being computed with the ONERA-elsA Reynolds-averaged Navier-Stokes (RANS) solver and the ONERA-ffd72 software. This paper exhibits the results of the new grid convergence process and buffet study (cases 1 and 2 of DPW-5). The impacts of the wing twist modification on drag and moment productions are investigated. The grid convergence study led with the as-tested shape in fully turbulent conditions gives an extrapolated drag value close to 254 counts, which is 4 counts higher than the drag produced by the original CFD geometry. Moreover, to further match the wind tunnel conditions, computations including a laminar zone up to 10% of the wing chord have been performed. These calculations with experimental wing twist and laminar / turbulent transition significantly improve the agreement between the numerical and experimental data.

[1] Engineer, Civil Aircraft Unit, Applied Aerodynamics Department, david.hue@onera.fr, AIAA Member.

Nomenclature

alpha	=	angle of attack
AR	=	aspect ratio
b	=	aircraft span
c	=	wing chord
CDf	=	friction drag coefficient
CDff	=	far-field drag coefficient
CDi	=	lift-induced drag coefficient
CDnf	=	near-field drag coefficient
CDp	=	pressure drag coefficient
CDsp	=	spurious drag coefficient
CDv	=	viscous drag coefficient
CDvp	=	viscous pressure drag coefficient
CDw	=	wave drag coefficient
Cf	=	skin friction coefficient
CL	=	lift coefficient
CM	=	pitching moment coefficient
Cp	=	pressure coefficient
Ma	=	Mach number
p	=	static pressure
Re	=	Reynolds number
Sref	=	reference surface area
u, v, w	=	x, y, z velocity components
Y^+	=	normalized first cell height
η	=	fraction of wing span
ρ	=	density
∞	=	subscript for freestream state value

I. Introduction

THE Drag prediction Workshop series was initiated in 2001 by a working group of the AIAA Applied Aerodynamics Technical Committee. The objective was to assess the state-of-the-art computational methods as practical aerodynamic tools for aircraft drag and moment predictions. Over the years, it has provided an impartial forum for evaluating the effectiveness of existing CFD codes and modelling techniques using Navier-Stokes solvers.

In 2012, the focus of the 5th AIAA CFD Drag Prediction Workshop was to continue studies with the CRM Wing-Body configuration investigated in DPW-4. The Applied Aerodynamics Department of ONERA participated in this new DPW, as it did in DPW-2 (2003) and DPW-4 (2009), a presentation [1] was given during the workshop held in News Orleans, Louisiana, in June 2012. For this occasion, NASA presented a paper [2] announcing that the experimental CRM model and the numerical geometry were slightly different. Indeed, when the wind tunnel model was tested, the wings twisted more than it was expected and did not match the nose-down twist of the geometry used for the computational studies. Such a difference of wing shapes could provoke non-negligible effects on the aerodynamic flow and especially on drag and pitching moment productions. Consequently, using a correct experimental wing twist, a whole CFD investigation has been carried out at ONERA, notably to reconsider the comparisons between numerical evaluations and experiments.

The publication of this work is the object of the present article. First, it gives the descriptions of the new CRM geometry and of the different grids which have been modified for the computations. ONERA CFD methods are briefly explained. Afterwards, a comparative grid convergence study is presented; wing twist modification impacts are highlighted. Then, a paragraph is dedicated to the ONERA computations including a laminar zone on the CRM wing. Finally, a buffet onset study is presented.

II. New CRM Geometry and Grids

A. New CRM Geometry

In the context of DPW-5 studies, only the wing/body/tail-off CRM configuration is considered. This relevant open geometry was designed by a Technical Working Group: "The Boeing Company took the lead on detailed aerodynamic design of the CRM, while NASA took the lead on model design, fabrication and testing of the CRM" [3]. As a result, the CRM configuration has the following characteristics: conventional low-wing configuration, possible nacelle/pylon installation, design Mach number of 0.85, fuselage representative of a wide/body commercial aircraft. Original geometry is shown in Fig. 1.

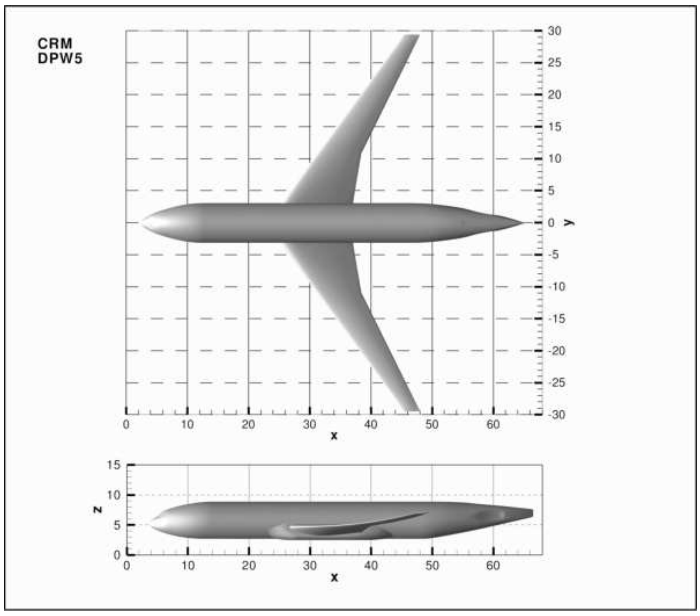

Fig. 1 CRM Wing-Body configuration.

The reference geometry is defined by mean-aerodynamic chord c = 7.00532 m, reference surface area *Sref* = 383.68956 m^2 (full-model), semispan $b/2$ = 29.38145 m, aspect ratio AR = 9.0, and moment center *Xref* = 33.67786 m, *Yref* = 0.0 m, and *Zref* = 4.51993 m.

As was written previously, studies carried out by NASA in 2012 revealed that the experimental model and the original numerical geometry have different wing twists. In reference [2], the wing twist of the as-tested shape is given. Table 1 presents these values and the ones of the original CFD shape. In the wingtip area, it can be noticed that the experimental model exhibits a nose-down twist greater of approximately 1 degree than the wing twist of the initial CFD version.

Table 1 Comparison of wing twists for the original CFD geometry and the as-tested model.

η	Original CFD geometry twist (°)	Measured model twist (°)
0.131	3.907	
0.201	2.963	
0.2765		1.547
0.283	1.745	
0.397	0.408	
0.4481		-0.803
0.502	-0.631	
0.5576		-1.794
0.603	-1.152	
0.727	-1.649	
0.7272		-2.739
0.846	-2.156	
0.9464		-4.108
0.950	-3.003	

B. Modified Common Multi-Block Grids

In 2012, the DPW-5 Committee provided a large number of grids and made them usable for all the participants. A family of point-matched multi-block grids for the CRM Wing-Body configuration was generated [4]. In this study, only the multi-block grid system has been used. The different characteristics of these meshes are indicated in Table 2:

Table 2 CRM; multi-block structured grids provided by the DPW Committee.

Level	Name	Hexahedra	Y^+
L1	Tiny	638,976	2.00
L2	Coarse	2,156,544	1.33
L3	Medium	5,111,808	1.00
L4	Fine	17,252,352	0.67
L5	Extra-Fine	40,894,464	0.50
L6	Super-Fine	138,018,816	0.33

Sizes of these grids range from 638,976 to 138,018,816 hexahedra, exhibiting a grid-size-ratio of 216. These meshes are O-type grids created by extrusion of the surface discretisation (see Fig. 2). They are made of 5 structured blocks. Through this strategy, a precise control on grid quality, such as grid spacing, stretching ratio and grid orthogonality near configuration surfaces is achieved. The normal spacing of the first cell next to the wall varies from Y^+ = 2.00 for the tiny grid to Y^+ = 0.33 for the super-fine mesh. The mesh extent is greater than 100 mean-aerodynamic chords. More details focusing on the particular topology of these grids are available in [4,5]. An illustration of the refinement levels is given in Fig. 3.

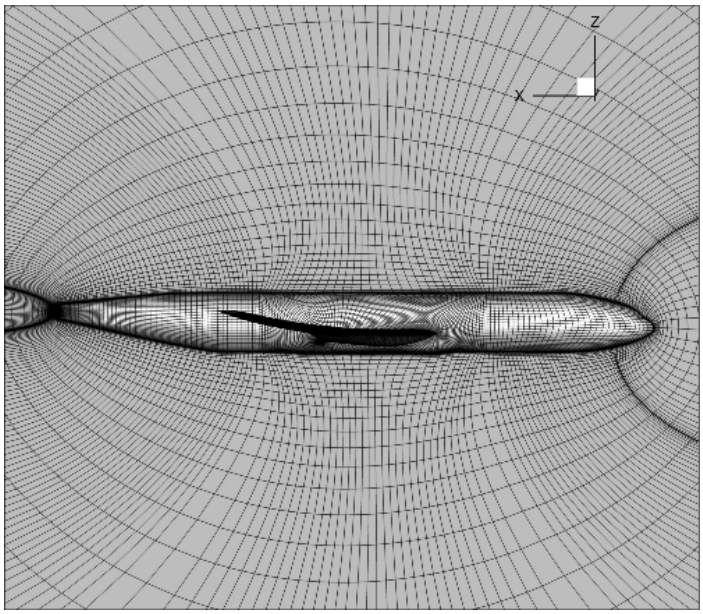

Fig. 2 CRM; O-type common MB grids; L1.

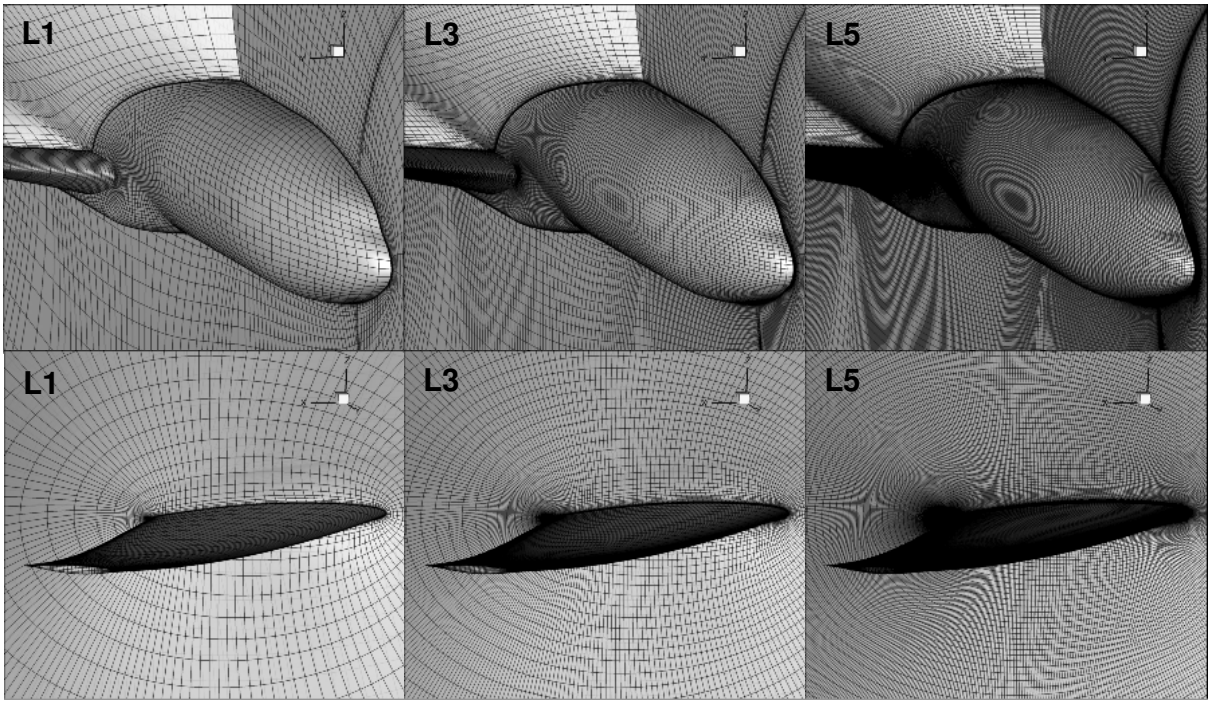

Fig. 3 CRM; common MB grids L1, L3, L5.

In order to match the as-tested shape presented in the previous paragraph, the common MB grids provided by the DPW Committee have been modified. As explained in reference [2], the objective was to "apply the twist increments to the airfoil sections and then to modify the surface and volume grids". In [2], the method used is "a linear shearing about the trailing edge as opposed to a true twist increment. As the absolute twist values are small and the largest twist increment is about one degree, any error introduced from the use of shearing would be much smaller than the measurement accuracy". In the study carried out at ONERA, an in-house grid deformation code was employed to implement the corrected wing twist in the new meshes. The twist increment at the root was set to zero. Then, the five experimental twist values at different η stations (see Table 1) were used to perform a Y-axis rotation of the wing about the trailing edge of the station concerned. Between these stations, linear rotation magnitude variations have been applied. As the CRM wing trailing edge is thick, the rotation point has been placed in its center. The two grid deformation methods can be considered as equivalent here. The new NASA geometry including wing twist correction has been compared to the one of ONERA: they are identical.

The as-tested shape obtained at ONERA is visible in Fig. 4 (in black); it is compared to the shape previously used for all the CFD studies (in grey). The geometrical discrepancy is particularly noticeable at the wingtip.

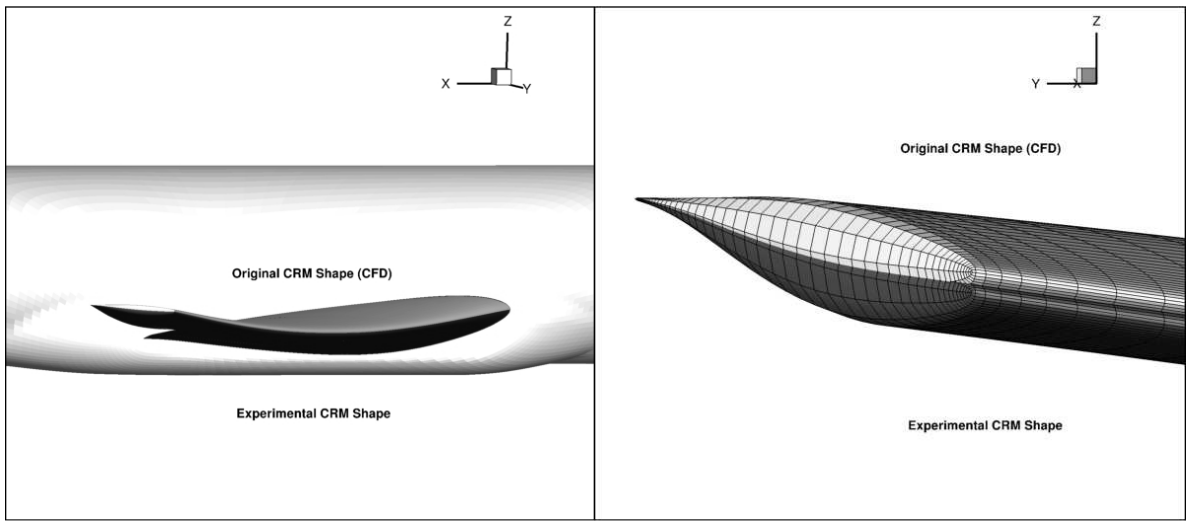

Fig. 4 CRM; comparison of original CFD and as-tested wing geometries.

In this paper, the grids that have been modified by the wing twist deformation process are named L1', L2', L3', L4', L5', and L6'. These meshes exhibit the same characteristics as the original common MB grids.

III. Solver and Far-Field Post-Processing

A. ONERA – elsA RANS Solver

Structured RANS computations are performed with the ONERA-elsA Navier-Stokes solver [6,7]. This software uses a cell-centered finite-volume discretization on structured and hybrid meshes. Time integration is carried out by a backward-Euler scheme with implicit LU-SSOR relaxation. Spatial discretization is realized using a central Jameson scheme with artificial viscosity. Multigrid techniques can be used to accelerate the convergence. Turbulence effects are simulated by the one-equation Spalart-Allmaras model. In this study, all the grids have been computed by the elsA code using the CGNS format.

In order to reach a satisfactory level of convergence, the computations were continued until the fluxes were stable enough to observe a lift variation inferior to +/- 0.001 and a drag variation inferior to 1 drag count over the last thousand of iterations (1 drag count = 10^{-4}).

The elsA simulations are executed on a Silicon Graphics cluster (SGI ICE 8200) composed of 4,992 cores representing a power of 57.9 teraflops. The computations carried out for this work have been performed in parallel mode, using from 4 to 256 cores.

The elsA software allows generating output extracts such as skin solutions (fluxes, pressure and friction repartitions, Y^+ mesh size…) and obviously flow solutions in the whole computational domain (conservative variables, stream traces…). Fig. 5 illustrates the capabilities of elsA, exhibiting the CRM configuration in cruise flight with its surface pressure distribution, iso-surfaces of Mach 1, and cutting planes showing the turbulent viscosity in the fuselage wake and the vorticity close to the wingtip.

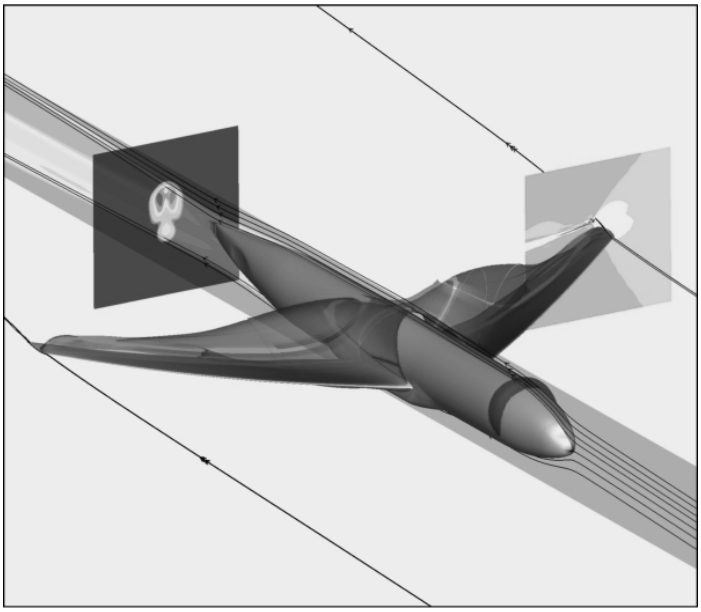

Fig. 5 CRM; *Ma* = 0.85, *Re* = 5 x 10^6, *CL* = 0.5; illustration of elsA capabilities.

B. ONERA – ffd72 Post-Processing Code: the Far-Field Approach

The formulations and methods relative to the far-field theory have been presented in former publications [8,9,10,11,12]. In this study, all the far-field analyses are carried out with the drag extraction software *ffd72*. This code is based on the formulations given in the references mentioned above.

This software was developed to provide a physical drag breakdown into viscous, wave, and lift-induced drag components and therefore to eliminate spurious drag by difference with the near-field drag coefficient. The code ffd72 is used at the end of the CFD process. It is a post-processing tool working on the numerical solutions provided by the solver.

The different drag coefficients which are used in this article are defined here:

$$CD_{nf} = CD_p + CD_f \quad \textbf{(1)}$$

$$CD_{ff} = CD_v + CD_w + CD_i \quad \textbf{(2)}$$

$$CD_{sp} = CD_{nf} - CD_{ff} \quad \textbf{(3)}$$

Spurious drag is defined as drag produced through entropy or stagnation enthalpy variations along streamlines outside physical viscous layers and shocks, and not resulting from vortex decay. The viscous pressure drag *CDvp* is also defined. It is the part of the viscous drag which is not due to the friction drag (displacement effect, flow separation…):

$$CD_v = CD_{vp} + CD_f \quad \textbf{(4)}$$

The far-field formulation allows for the following near-field/far-field drag balance:

$$CD_p + CD_f = CD_v + CD_w + CD_i + CD_{sp} \quad \textbf{(5)}$$

Fig. 6 illustrates some of the capabilities of the far-field post-processing code ffd72. It shows the control volumes for the viscous drag (about the plane surface and wake) and for the wave drag (in black along the upper part of the wing) of the CRM configuration in cruise flight.

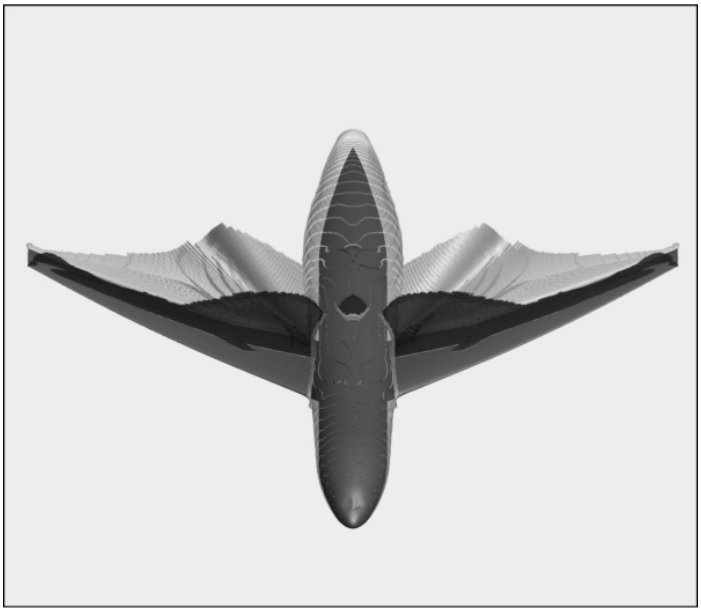

Fig. 6 CRM; Ma = 0.85, Re = 5 x 10^6, CL = 0.5; illustration of ffd72 capabilities.

IV. Grid convergence study, laminar / turbulent calculation, Experimental / Numerical confrontation

The grid convergence study presented in this paper basically corresponds to the DPW-5 case 1. However, the geometry and the grids which have been used here are the ones matching the as-tested shape. The aerodynamic conditions are the following: Mach number *Ma* = 0.85, lift coefficient *CL* = 0.5 (±0.001), and Reynolds number *Re* = 5 x 10^6. NASA Ames and NTF transonic wind tunnel tests matched these conditions. All the drag coefficients are given in drag counts (1 drag count =10^{-4}).

A. Grid convergence study with the correct Experimental Wing Twist

All these computations were performed in fully turbulent conditions. A target lift algorithm has been used to reach the requested lift coefficient accuracy *CL* = 0.5 (±0.001). The grids L1' and L3' were computed without multigrid techniques, respectively on 4 and 16 cores. The grids L2', L4', L5', and L6' were calculated with only one level of coarse grid for the multigrid algorithm, respectively on 8, 48, 96, and 256 cores. As the convergence criteria were long to achieve with these O-type grids, large numbers of iterations were performed to complete these computations (10,000 to 20,000 iterations), as it can be observed in Fig. 7.

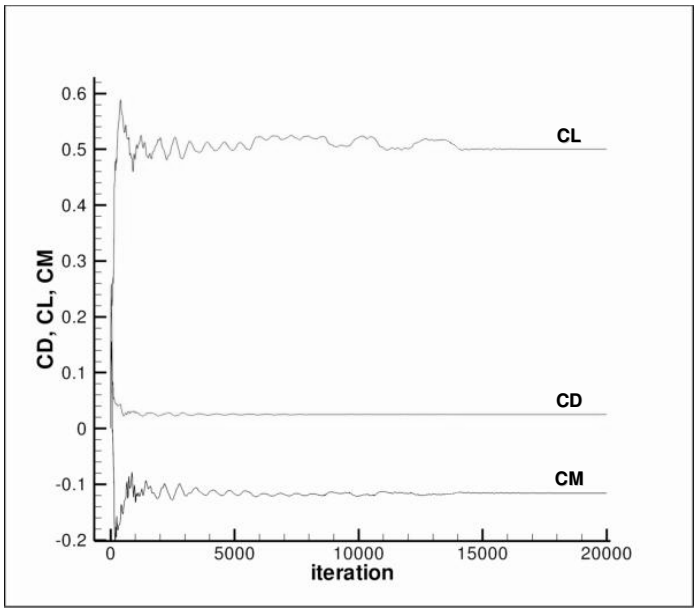

Fig. 7 CRM; grid convergence study with new MB grids (*Ma* = 0.85, *Re* = 5 x 10^6, *CL* = 0.5); grid L3'; illustration of the convergence process (target lift algorithm).

The results of this new grid convergence study are summarized in Table 3 and Table 4. Table 3 gives the angles of attack and the near-field drag and pitching-moment coefficients obtained with the elsA solver for each grid level. Table 4 presents the far-field analyses and therefore the drag coefficients given by the ffd72 code. All the drag components are defined in the previous part.

Table 3 CRM; grid convergence study with new MB grids (*Ma* = 0.85, *Re* = 5 x 10^6, *CL* = 0.5); angles of attack, lift, near-field drag, and pitching moment coefficients from elsA.

Grid level	L1'	L2'	L3'	L4'	L5'	L6'
Alpha	2.721	2.675	2.657	2.640	2.637	2.637
CL	0.4999	0.4997	0.4998	0.4994	0.4995	0.4999
CDnf	265.4	258.2	256.3	254.6	254.2	254.1
CDp	151.7	144.5	142.2	140.1	139.5	139.2
CDf	113.7	113.7	114.0	114.5	114.7	114.9
CM	-0.084	-0.087	-0.088	-0.0895	-0.0899	-0.0903

Concerning Table 3 and Fig. 8, the following comments can be made:

1) Even if a large number of iterations was necessary, the target lift algorithm managed to achieve a high precision concerning the lift coefficient for each grid level. A variation of 0.084° of the angle of attack is observed between the coarsest grid (L1') and the finest ones (L5' and L6'). This variation is similar to the one observed with the original common MB grids. However, the angle of attack required to reach the cruise lift coefficient (*CL* = 0.5) is about 0.5° higher than it was with the former wing.

2) The converged value of total drag for the as-tested CRM Wing-Body configuration in these aerodynamic conditions is 254 drag counts. In the former study [1,5], the original grid convergence process gave a value close to 250 counts. The wing twist deformation (stronger nose-down twist) generated a non-negligible increase of 4 counts of the aircraft drag for the same lift coefficient.

3) A pressure drag decrease of 12.5 counts due to grid refinement is recorded between L1' and L6'. This can be explained by a better discretization of the computational domain which leads to a more accurate solution and a weaker artificial dissipation. The *CDp* converged value is 139 drag counts. Given the fact that this component was equal to 135 counts with the original CFD shape, it is obvious that the impact of the wing twist modification is concentrated on pressure drag. The grid refinement does not seem to have significant effects on the drag increase due to the greater nose-down twist (see Fig. 8).

4) The variation of the friction drag coefficient is really limited (an increase of only 1.2 drag counts is observed between L1' and L6' levels) and this coefficient is almost not affected by the geometry modification.

5) Considering the very similar coefficients obtained with the grids L4', L5', and L6' and taking into account the standard expected accuracy of drag and pitching moment predictions, it may be said that the L4' level (17 million elements) is sufficient to evaluate the global aerodynamic forces and moments with a satisfactory precision.

Concerning Table 3 and Fig. 9, it can be observed that:

1) The pitching moment varies from -0.084 for the coarsest grid to -0.090 for the finest one, exhibiting a variation of about 6 thousandths. This *CM* variation is the same as the one exhibited by the former grid convergence study.

2) The impact of the twist modification on the pitching moment coefficient is substantial. The original *CM* component is reduced of almost 25% of its absolute value, moving from -0.1175 to -0.090. The consequences of this new CFD evaluation on the agreement between the experimental and numerical data will be discussed in the next part.

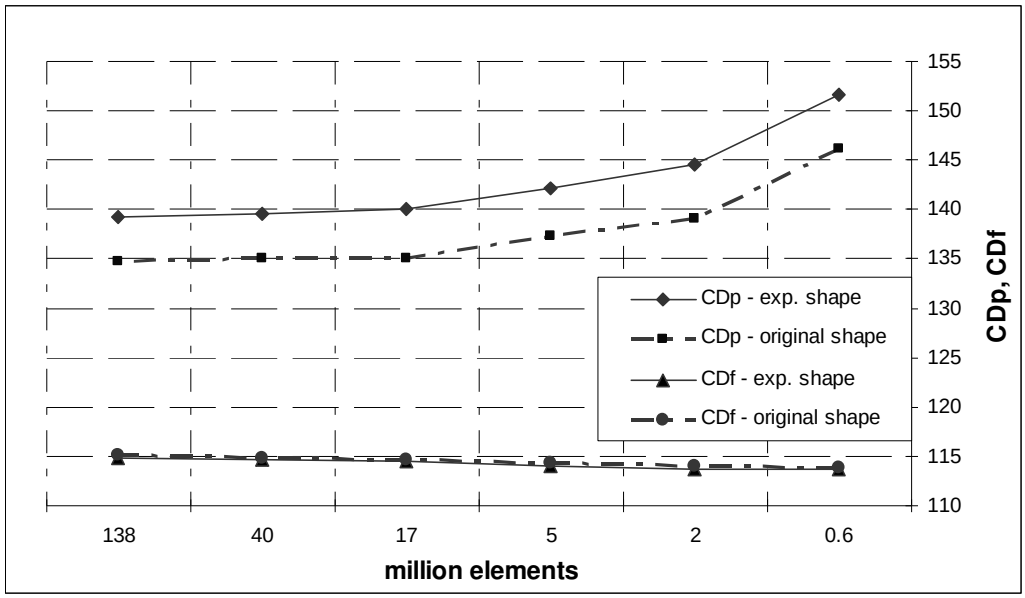

Fig. 8 CRM; grid convergence study with new MB grids (*Ma* = 0.85, *Re* = 5 x 10^6, *CL* = 0.5); pressure drag, and friction drag versus mesh refinement.

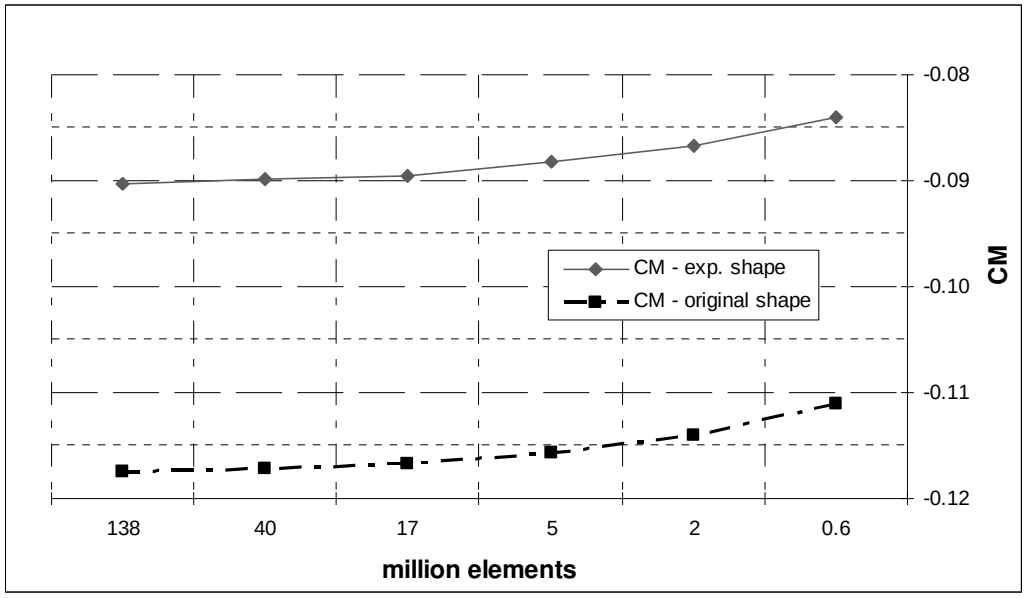

Fig. 9 CRM; grid convergence study with new MB grids (*Ma* = 0.85, *Re* = 5 x 10^6, *CL* = 0.5); pitching-moment versus mesh refinement.

The far-field drag analyses are presented in Table 4. The lift and total near-field drag coefficients are given. Then, the friction and the viscous pressure drags are detailed; the sum of these two components corresponds to the viscous drag. As said previously, the total far-field drag *CDff* is the sum of the viscous drag *CDv*, the wave drag *CDw*, and the induced drag *CDi*. Finally, the spurious drag *CDsp* is the difference between the near-field drag and the far-field drag.

Table 4 CRM; grid convergence study with new MB grids (*Ma* = 0.85, *Re* = 5 x 10^6, *CL* = 0.5); far-field analyses from ffd72.

Grid level	L1'	L2'	L3'	L4'	L5'	L6'
CL	0.4999	0.4996	0.4998	0.4994	0.4995	0.4999
CDnf	265.5	258.4	256.4	254.7	254.2	254.2
CDf	113.9	113.7	114.0	114.5	114.7	114.8
CDvp	46.3	43.5	42.3	41.3	40.9	40.6
CDv	160.0	157.2	156.3	155.8	155.5	155.4
CDw	6.6	5.9	5.7	5.7	5.7	5.8
CDi	94.3	93.6	93.4	92.9	92.8	92.9
CDff	260.9	256.7	255.5	254.3	254.0	254.1
CDsp	4.6	1.7	0.9	0.4	0.1	0.1

The grid convergence study shows the following:

1) The mesh refinement produces a nonnegligible effect on the viscous drag prediction, with a decrease of 4.6 drag counts from L1' to L6'. The viscous pressure drag coefficient itself is submitted to a decrease of 5.7 drag counts. The values of these coefficients are almost not impacted by the wing twist increment.

2) A very limited variation is observed for the wave drag component from L1' to L6' with a decrease of only 0.8 count. This component does not seem to be as sensitive to the grid refinement as *CDvp* is. However, its sensitivity to the wing twist modification is really significant. As it can be noticed in Fig. 10, the original *CDw* coefficient of about 4 counts is increased of almost 50%. Indeed, the new wing geometry produces a wave drag of about 6 counts.

3) The lift-induced drag component exhibits a decrease of 1.4 drag counts due to the grid refinement. In addition, Fig. 10 shows that the induced drag coefficient is also increased because of the wing twist deformation. The value obtained with the new grid convergence process is close to 93 drag counts, which is more than 2 counts higher than the former value.

4) The greatest value of spurious drag is 4.6 drag counts. It is obviously obtained with the 1st grid level L1'. On the other hand, the grids L5' and L6' produce almost zero spurious drag.

The far-field approach allows establishing the following statistics: the viscous drag represents 61.2% of the aircraft drag (74% of *CDv* are due to the friction drag and the remaining 26% come from the viscous pressure drag). The wave drag corresponds to only 2.3% of total drag while the lift-induced drag is responsible for 36.5% of the aircraft drag. Furthermore, the increase of about 4 counts in pressure drag due to the wing twist correction comes from a 50/50 contribution of wave drag and lift-induced drag increases (see Fig. 10).

As a partial conclusion, this new grid convergence study using the as-tested CRM shape shows interesting results concerning the wing twist modification effects. The far-field approach allowed determining the physical sources of the drag increase which has been observed.

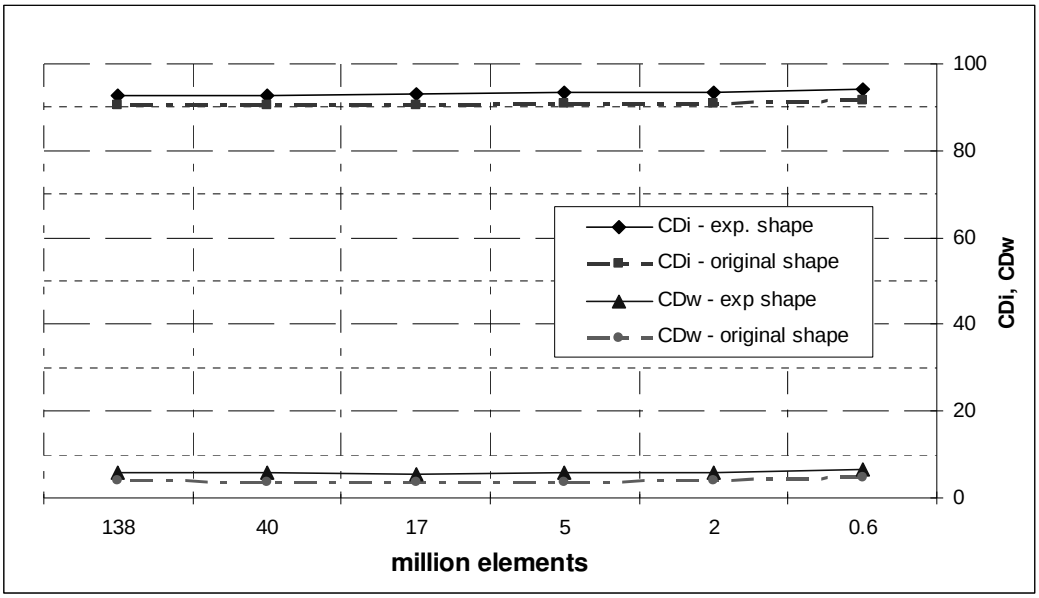

Fig. 10 CRM; grid convergence study with new MB grids (*Ma* = 0.85, *Re* = 5 x 10^6, *CL* = 0.5); lift-induced drag and wave drag versus mesh refinement.

The following comments and figures deal with local analyses. These investigations lead to a deeper understanding of the wing twist correction impact on drag productions. Taking into account the previous results, the grid L4' has been chosen for these local studies: it is sufficiently fine to obtain accurate data. First, Fig. 11 exhibits the pressure distribution along the chord at 50% and 95% of the wingspan for the original and experimental shapes. For the midspan section, it can be noticed that the *Cp* distributions of both geometries are very similar. Nevertheless, the shock is slightly stronger with the experimental shape, which is in agreement with the increase of 2 drag counts observed for the *CDw* coefficient (see Fig. 10 and Table 4). The section located at 95% of the wingspan shows quite different features especially on the suction side. The main shock location is identical for both wing shapes but the shock system is different. The original shape presents a first recompression from 35 to 40% chord whereas the experimental wing produces a much weaker first recompression close to 25% chord but then a stronger shock. Fig. 12 perfectly illustrates these comments by exhibiting the *CDw* control volumes given by ffd72 over the wing of both geometries.

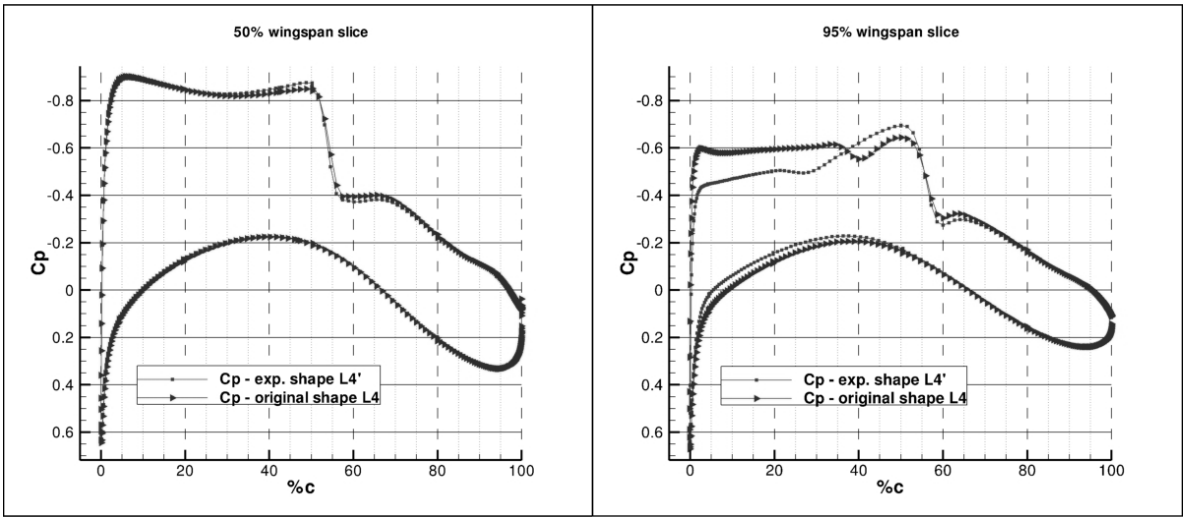

Fig. 11 CRM; *Ma* = 0.85, *Re* = 5 x 10^6, *CL* = 0.5; grids L4' / L4; numerical *Cp* distribution along the chord at 50% and 95% of wingspan.

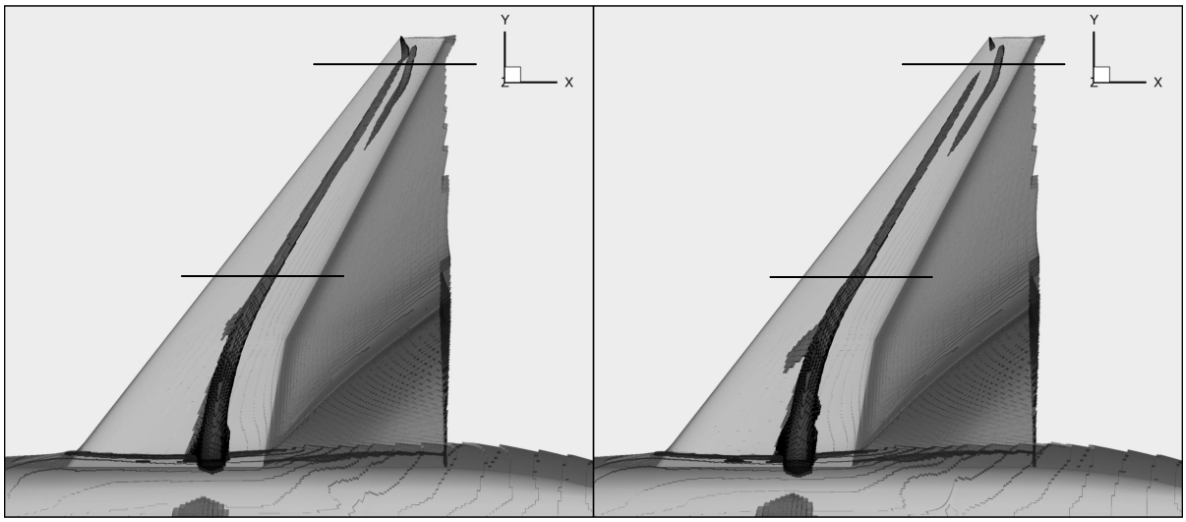

Fig. 12 CRM; *Ma* = 0.85, *Re* = 5 x 10^6, *CL* = 0.5; grids L4' / L4; viscous (grey) and wave (black) drag control volumes for the original shape (left) and the experimental shape (right).

The far-field extraction code ffd72 is also able to produce the spanwise productions of the different physical drag coefficients. As the increase of 4 counts in total drag due to wing twist correction is caused by a 50/50 contribution of wave and lift-induced drag increases, Fig. 13 focuses on these two components. It shows the *CDi* and *CDw* spanwise productions for the original and the experimental geometries. Concerning the curves of wave drag productions, it can be observed that the stronger shock generated at midspan by the experimental shape is clearly detected by ffd72. It is perfectly in agreement with Fig. 11 and Fig. 12. The curves of induced drag productions should be interpreted as transcriptions of the span load distributions. Focusing on the external part of the wing (y > 20 m), it can be said that the stronger nose-down twist of the experimental shape induces a lower local incidence implying lower loads in this area. As a consequence, the contribution to the lift-induced drag coefficient of the external wing is lower for the experimental geometry than it is for the original one. On the other hand, as the computations are performed in iso-*CL* conditions, the internal part of the experimental wing (y < 20 m) needs to compensate the loss of load described above. That is why, the internal wing of the as-tested shape exhibits a contribution to *CDi* stronger than the original geometry. The span load distribution of the wind tunnel shape is not as good as the original one and generates an increase of more than 2 counts of the lift-induced drag component. As a conclusion, it can be said that, in iso-*CL* conditions, the twist correction applied to match the experimental shape leads to non-negligible modifications of the wing flowfield.

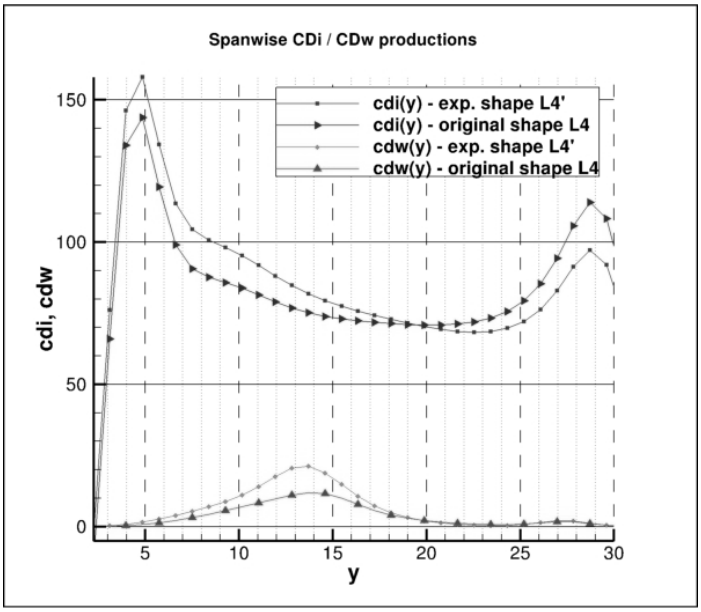

Fig. 13 CRM; *Ma* = 0.85, *Re* = 5 x 10^6, *CL* = 0.5; grids L4' / L4; *CDi* and *CDw* spanwise productions.

B. Laminar / Turbulent computation

During the experimental investigation of the CRM conducted in the NASA National transonic Facility, the Wing-Body configuration was equipped of trip dots installed at 10% chord [2]. The objective was to apply a reliable method to fix transition on the model. For a Reynolds number of 5 millions, the flow was assumed to be entirely laminar before the trip dots. As stated in the conclusions of [15], the experimental skin friction levels on the wing leading edge (forward the trip dots at 10% chord) are therefore much smaller than those computed using a fully turbulent assumption. Contrary to the former ones, the computation presented in this paragraph was performed with a laminar zone matching the one obtained in the experiments.

The aerodynamic conditions are identical to the ones used for the convergence study: Mach number $Ma = 0.85$, lift coefficient $CL = 0.5$ (± 0.001), and Reynolds number $Re = 5 \times 10^6$. A target lift algorithm has been used to reach the requested lift coefficient accuracy $CL = 0.5$ (± 0.001). As it has given results which are satisfactory in terms of accuracy, only the grid L4' was used for this computation. It was calculated on 48 cores with one level of coarse grid for the multigrid algorithm. The convergence criteria were respected.

The solver elsA allows calculating or specifying the transition location over a surface. In this case, a laminar zone is imposed up to 10% chord on both sides of the wing. The fuselage remains entirely turbulent. As an illustration, Fig. 14 shows the friction levels on the suction side for the laminar / turbulent calculation. The previous fully turbulent computation results are added for comparison purposes. It can be observed that the laminar zone imposed up to 10% chord dramatically reduces the friction modulus at the leading edge of the wing. This laminar region has an important impact on the wing flowfield. The friction drag component is not the only one to be affected.

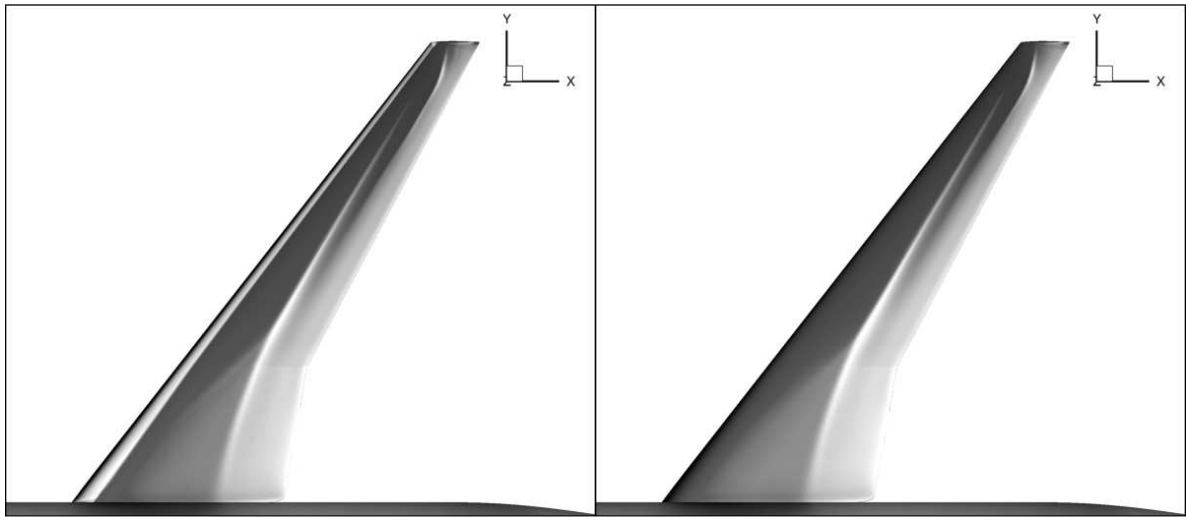

Fig. 14 CRM; *Ma* = 0.85, *Re* = 5 x 10^6, *CL* = 0.5; grid L4'; friction modulus for laminar / turbulent (left) and fully turbulent (right) computations.

The drag analyses for the laminar / turbulent case are presented in Table 5. The lift and total near-field drag coefficients are given. Then, the far-field drag components are detailed. The second column of Table 5 corresponds to the equivalent fully turbulent computation. The last column represents the difference between the first one and the second one for each variable. It clearly highlights the physical impacts of the laminar zone.

Table 5 CRM; laminar / turbulent computation with the grid L4' (*Ma* = 0.85, *Re* = 5 x 10^6, *CL* = 0.5); aerodynamic coefficients from ffd72.

Grid level	L4' laminar / turbulent computation	L4' turbulent computation	Δ
Alpha	2.582	2.640	-0.058
CL	0.4999	0.4994	0.0005
CDnf	248	254.7	-6.7
CDp	136.5	140.2	-3.7
CDf	111.5	114.5	-3.0
CM	-0.0936	-0.0895	-0.0041
CDvp	38.5	41.3	-2.8
CDv	150	155.8	-5.8
CDw	4.8	5.7	-0.9
CDi	92.9	92.9	0.0
CDff	247.7	254.3	-6.6
CDsp	0.3	0.4	-0.1

The drag analyses show the following:

1) The total near-field drag decrease is equal to 6.7 counts. It is very close to the change of 2% expected in the conclusions of [15]. The friction drag is responsible for about 45% of this decrease while the pressure drag drop represents the remaining 55%. The pitching moment is slightly modified by the presence of the laminar region.

2) Concerning the far-field coefficients, it can be observed that the greatest part (87%) of the total drag decrease is due to a significant drop of the viscous drag, the friction and the viscous pressure components being the most affected ones. The wave drag coefficient is also reduced: it is almost one count smaller in laminar / turbulent conditions.

As a consequence, the numerical drag value obtained by ONERA for the as-tested CRM Wing-Body configuration is now 247.7 drag counts.

C. Experimental / Numerical Confrontation of Drag and Moment Evaluations at design point

This part is aimed at comparing the experimental results of NASA to these new RANS calculations carried out with the appropriate twist correction and the laminar leading edge of the wing. As mentioned above, the original CFD wing geometry of DPW-4 and DPW-5 did not match the twist distribution of the wind tunnel model in test conditions; the updated shape used in this numerical study does. As a consequence, comparisons are now more meaningful. It seems that discrepancies may remain between the experimental and numerical wing bending distributions; nevertheless the effects should be very limited.

Fig. 15 summarizes all the comparisons explained in the following paragraphs. First, concerning the angle of attack which leads to a lift coefficient of 0.5, a significant discrepancy was observed between the original CFD Wing-Body geometry and the NASA wind tunnel model. Indeed, the NTF data exhibits an angle of attack of 2.8° to reach a *CL* coefficient of 0.5 [14] whereas an angle of only 2.15° was necessary for the original CFD shape [5]. The new CFD as-tested geometry needs an angle of attack close to 2.6° for the specified lift level (see Fig. 15). The agreement between experimental and numerical approaches is significantly improved.

Then, concerning drag prediction at design point (DPW-5 case 1), the ONERA grid convergence study performed with the CRM Wing-Body as-tested shape presented in this paper leads to the value of 254 drag counts (see Table 4). Moreover, the computation carried out with a laminar zone up to 10% of the wing chord gives a drag value of 247.7 counts (see Table 5). The experimental drag evaluation from NTF given in 2011 [14] provides a value of 248 counts (run 44). As it can be observed in Fig. 15, the latest numerical drag prediction from ONERA and the NASA measurement are now in almost perfect agreement.

Considering the pitching moment, this CFD study leads to a value close to -0.090 (see Fig. 15). The NTF experimental value is equal to -0.0625. The wing twist modification applied in order to match the as-tested shape improves significantly the agreement between the numerical prediction and the NTF measurement. Indeed, when the original CFD studies exhibited a *CM* value close to -0.1175 [5], the absolute discrepancy CFD / experiments (0.055) was substantial. The wing twist correction used here allows reducing this absolute difference by half. The remaining discrepancy could be explained by the interactions generated by the experimental mounting system.

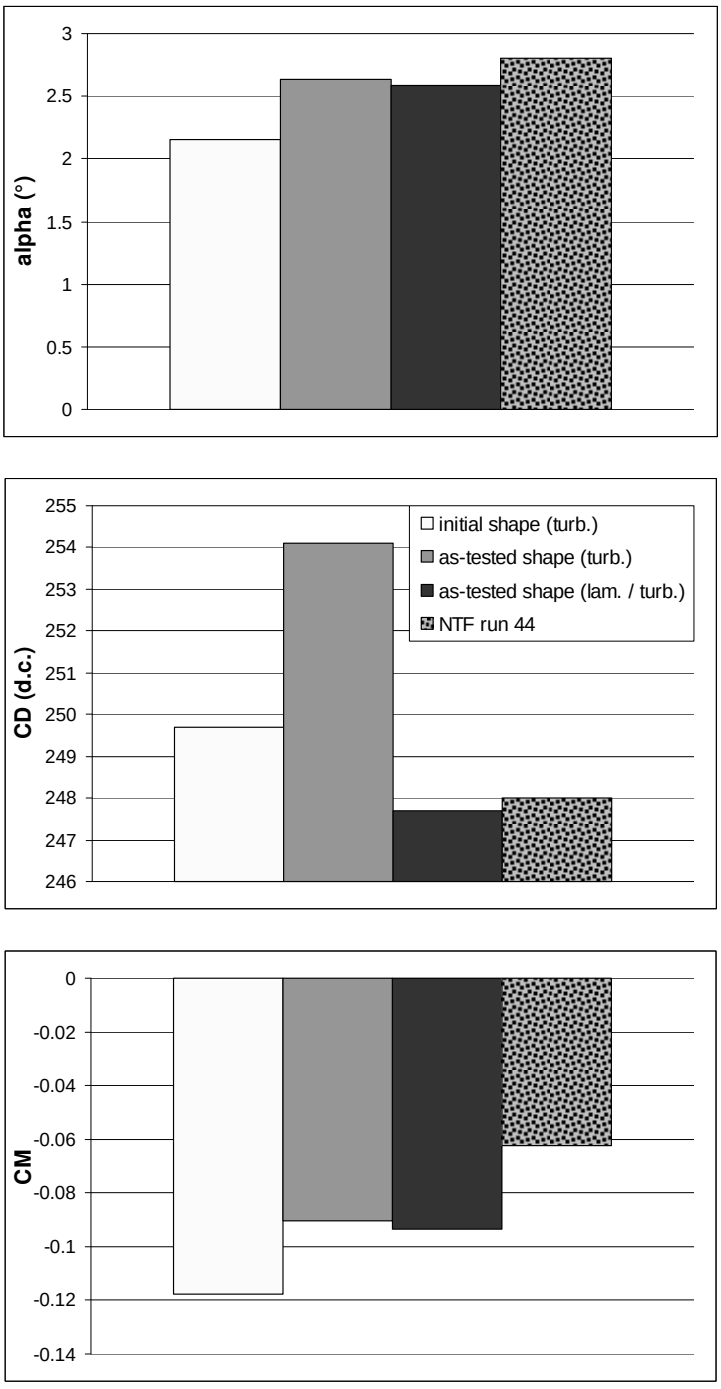

Fig. 15 CRM; *Ma* = 0.85, *Re* = 5 x 10^6, *CL* = 0.5; experimental vs. numerical (grids L4' / L4) data: *alpha*, *CD*, *CM*.

Finally, concerning the *Cp* distributions, wind tunnel data is available in [16]. Fig. 16 shows the comparison between the experimental (NTF run 44) and numerical pressure distributions for two sections located at 50 and 95% of wingspan. The computation used here corresponds to the grid L4' (as-tested shape) in fully turbulent conditions (the *Cp* distributions given by the laminar / turbulent computation being very similar). As the experiments were not realized in target-*CL* conditions, two angles of attack, surrounding the one which would lead to *CL* = 0.5, are presented. It can be seen that the number of pressure measurements in the middle part of the suction side is quite limited. As it can be observed for both wing sections, the agreement on the pressure side is quite satisfactory. On the upper side, for the section at 50% wingspan, the measured suction seems to be slightly stronger than the computed one before the shock and weaker after. Considering the section at 95% wingspan and more particularly the area of the suction side located before the shock position, it can be said that the agreement is significantly improved by the wing twist correction (see Fig. 11).

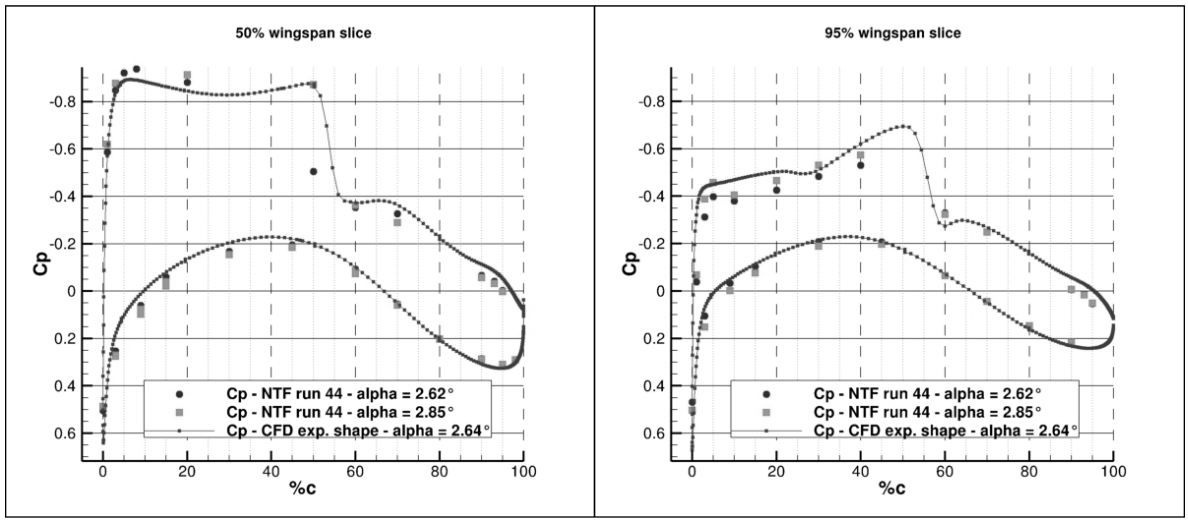

Fig. 16 CRM; *Ma* = 0.85, *Re* = 5 x 10^6, *CL* = 0.5; experimental vs. numerical (grid L4') *Cp* distributions along the chord at 50% and 95% of wingspan.

V. Angle of Attack sweep and Buffet onset studies

The angle of attack sweep and buffet onset studies presented in this paper correspond to the DPW-5 case 2. The geometry is still the as-tested CRM Wing-Body configuration. The aerodynamic conditions are the following: Mach number Ma = 0.85 and Reynolds number Re = 5 x 10^6. The *alpha* sweep aimed at exploring the buffet area in this article is defined by 8 points : 1.00°, 1.50°, 2.50°, 2.657°, 3.00°, 3.50°, 3.75°, and 4.00°.

Only the medium grid L3' presented above is used for this buffet study (as specified in the DPW-5 case 2). All the computations are fully turbulent. The strict convergence criteria have been ensured.

A. Angle of Attack sweep – Experimental / Numerical comparisons

The results of the *alpha* sweep study are summarized in Table 6. It presents the lift and near-field drag values, the pitching-moment coefficient, as well as the lift-to-drag ratio obtained with the elsA solver for each angle of attack. It can be noticed that the design point corresponding to CL = 0.5 is also given.

Table 6 CRM; alpha sweep study with the grid L3' (Ma = 0.85, Re = 5 x 10^6); angles of attack, lift, near-field drag, and pitching moment coefficients from elsA.

alpha	1.00	1.50	2.50	2.657	3.00	3.50	3.75	4.00
CL	0.2705	0.3367	0.4768	0.4998	0.5498	0.6114	0.6326	0.6508
CDnf	180.0	195.9	244.5	256.3	287.1	347.5	384.2	424.5
CDp	64.2	80.3	130.1	142.2	173.9	236.0	273.6	314.7
CDf	115.8	115.6	114.4	114.0	113.2	111.5	110.7	109.9
CM	-0.0639	-0.0710	-0.0855	-0.0882	-0.0950	-0.0991	-0.0947	-0.0883
CL/CD	15.0	17.2	19.5	19.5	19.2	17.6	16.5	15.3

Concerning Table 6, the following comments can be made:

1) The angle of attack varies from 1.00° to 4.00°. It implies a CL increase showing values from about 0.27 to 0.65. Fig. 17 presents the associated lift polar. The flow separations appearing on the wing when increasing the angle of attack induce a decrease of the lift coefficient relative to the theoretical straight line of the linear zone. Nevertheless, aerodynamic stall does not appear. In Fig. 17, the experimental data available in [16] and the numerical results of the original CFD shape [5] are added for comparison purposes. As was written previously, the lift polar is substantially modified by the wing twist correction. It can be observed in Fig. 17 that the CFD experimental shape exhibits a lift polar almost in perfect agreement with the NTF measurements, which was not the case with the original shape provided for DPW-4 and DPW-5.

2) The pressure drag increase is substantial when sweeping from 1.00° to 4.00° of incidence. Its value passes from 64 drag counts to almost 315 counts. On the other hand, the *alpha* sweep produces a quite limited variation of the friction drag coefficient. The cruise value of 114 counts slightly decreases to 110 at 4.00° of incidence. The massive flow separations on the wing surface are responsible for this *CDf* decrease. The total drag polar is shown in Fig. 18. The agreement between experimental and numerical results is quite satisfactory. The drag increase due to wing twist correction can be seen for the different lift levels.

3) The pitching moment coefficient variation describes a curve showing a minimum of about -0.1 for an angle of attack of 3.50°.

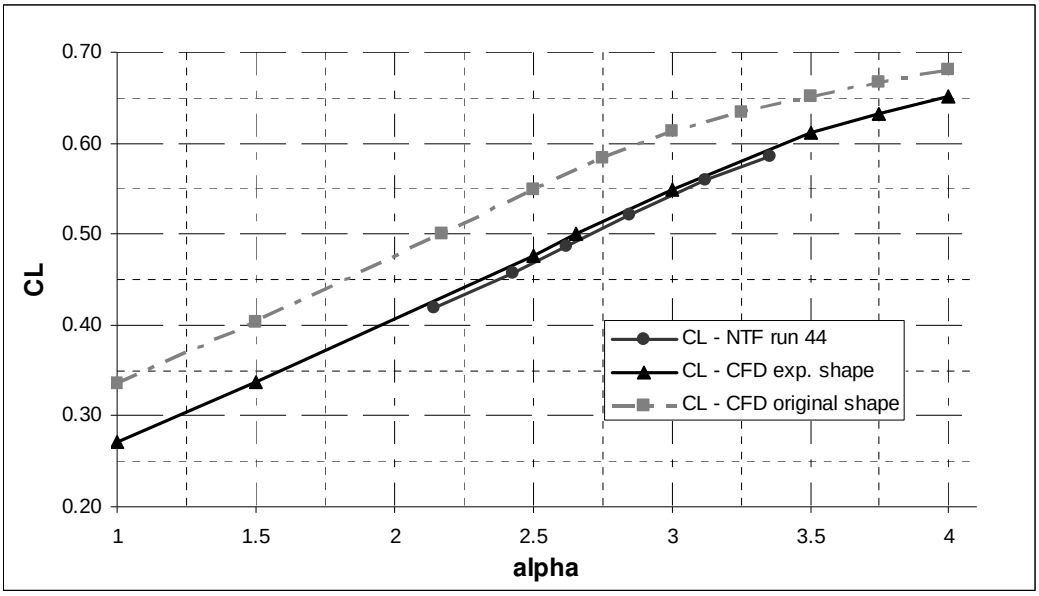

Fig. 17 CRM; alpha sweep study with the grid L3' (*Ma* = 0.85, *Re* = 5 x 10^6); lift polar.

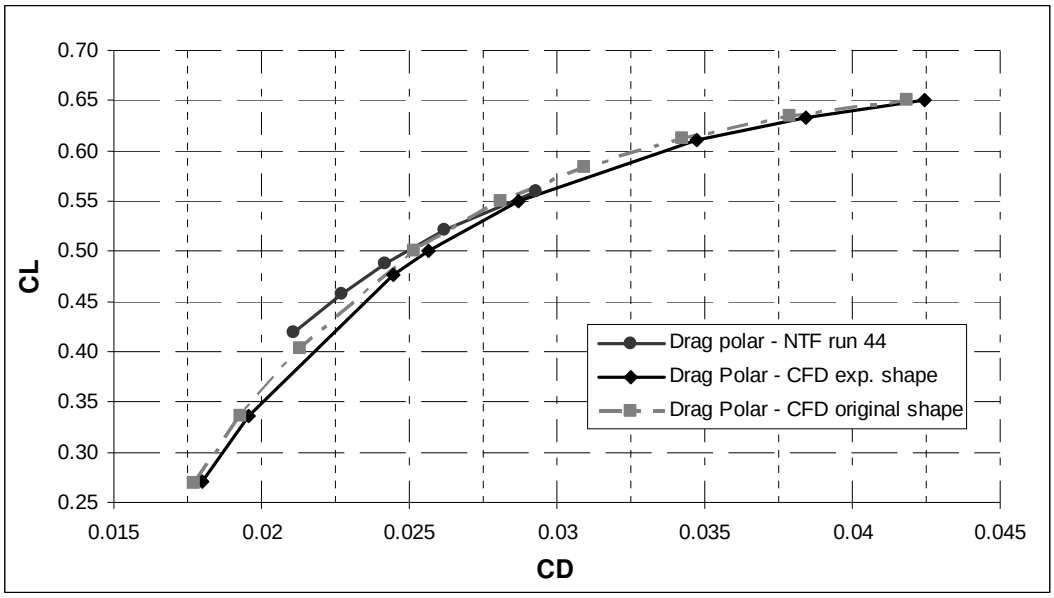

Fig. 18 CRM; alpha sweep study with the grid L3' (*Ma* = 0.85, *Re* = 5 x 10^6); drag polar.

B. Buffet onset study

A buffet onset study based on a global criterion is presented in this paragraph. For a transport aircraft, buffet phenomena correspond to possible vibrations which may occur during maneuvers at cruise speed. Depending on the angle of attack, flow separations over the wing can appear and excite the structure to a point where the flight safety is no longer guaranteed. For flight certifications, the aircraft is supposed not to encounter any buffet phenomena in the range [*CL*design; *CL*design + 30%].

A standard buffet onset indicator derived from the lift polar has been used in order to determine the angle of attack and the associated lift coefficient from which buffet is expected to exist. Considering the $CL(\alpha)$ curve in Fig. 19, the criterion "$\Delta\alpha = 0.1°$" is employed. A straight line can be defined following the slope of the *CL* linear zone. Conserving this slope, the straight line is then translated of $+\Delta\alpha$ in the alpha direction. The intersection between the *CL* curve and the new straight line provides the position of the buffet zone beginning. As it can be seen in Fig. 19, for the as-tested shape, this indicator gives the following couple $(\alpha_{buffet}\ ; CL_{buffet}) \approx (3.65°; 0.625)$.

At cruise Mach, according to this indicator, for angles of attack or lift coefficients stronger than (3.65°; 0.625), buffet is likely to occur. Considering the aircraft certifications, the lift coefficient being equal to 0.5 in cruise flight, the addition of a 30% margin would lead to a lift level of 0.65. For this Wing-Body configuration, the RANS computations carried out with the medium grid l3' and the Spalart-Allmaras turbulence model show that buffet phenomena over the CRM wing seem to appear for values lower than the one recommended in the certification rules.

In Fig. 19, the "$\Delta\alpha = 0.1°$" indicator is also applied to the original CFD shape [5]. As it can be observed, only the value α_{buffet} is modified. The lift coefficient CL_{buffet} is not affected.

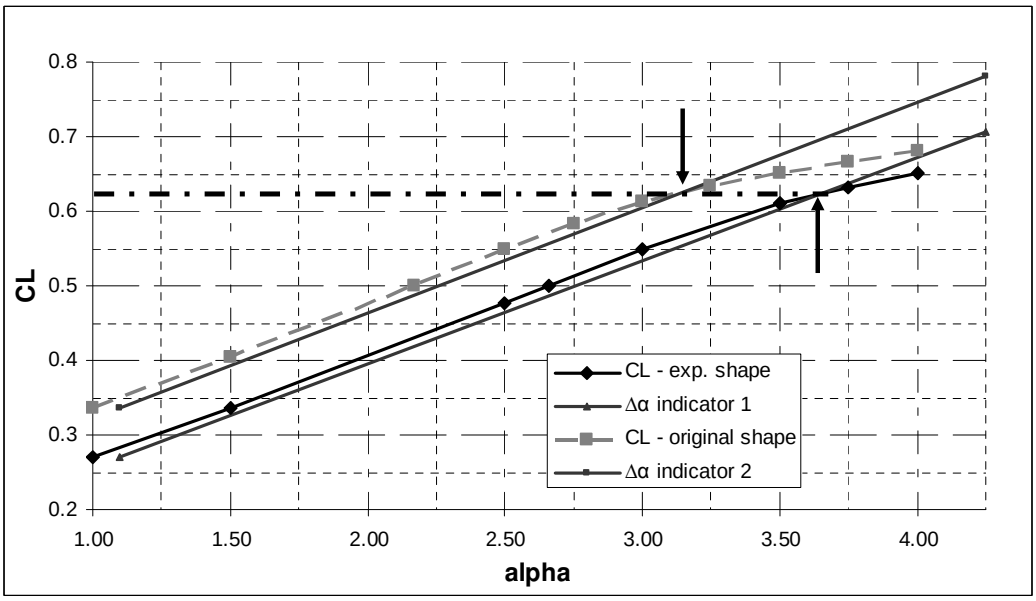

Fig. 19 CRM; buffet onset study with the grid L3' (*Ma* = 0.85, *Re* = 5 x 10^6); *CL* = f(*alpha*); $\Delta\alpha$ criterion.

VI. Conclusions

This paper is focused on the computational studies which have been performed at ONERA in 2013 in the framework of the 5th AIAA Drag Prediction Workshop. In 2012, NASA presented a paper announcing that the experimental CRM model and the original numerical geometry were slightly different: when the wind tunnel model was tested, the wings twisted more than it was expected and did not match the nose-down twist of the wing geometry used for the computational studies of DPW-4 and DPW-5. Such a difference of wing shapes could provoke non-negligible effects on the aerodynamic flow and especially on drag and pitching moment productions. Consequently, using a corrected wing twist, new CFD investigations have been carried out at ONERA, notably to reconsider the comparisons between numerical and experimental evaluations.

The results shown in this paper illustrate the current capabilities of RANS solvers to compute the drag and moment coefficients of transport aircraft in cruise conditions. A grid convergence process and a buffet onset study have been completed. To further match the wind tunnel conditions, computations including a laminar zone up to 10% of the wing chord have been performed. Interesting comparisons with experimental data have been presented. To achieve this work, the common MB grids provided by the DPW-5 Committee have been modified. The adequate wing twist correction has been applied to generate an as-tested shape. All these meshes have been computed with the ONERA-elsA solver using the Spalart-Allmaras turbulence model on a SGI supercomputer. Far-field drag analyses have been performed with the ONERA-ffd72 software.

Considering the pitching moment, the new CFD study has led to a value close to -0.090 while the NTF measurement is close to -0.0625. The wing twist modification applied in order to match the experimental shape has reduced by half the difference between the numerical moment value and the wind tunnel data. The remaining discrepancy could be explained by the interactions generated by the experimental mounting system.

The alpha sweep and buffet onset studies have allowed confirming that the lift polar has been substantially modified by the wing twist correction. The new CFD as-tested shape gave a lift polar almost in perfect agreement with the NTF measurements, which was not the case for the original geometry provided for DPW-5.

The grid convergence study for the CRM Wing-Body configuration at design point carried out with the corrected wing twist has exhibited a converged value of total drag close to 254 drag counts. The original geometry of DPW-5 gave a drag value of about 250 counts (CFD median of all DPW-5 participants). The far-field approach has allowed determining that the increase of 4 counts in drag due to the wing twist correction comes from a 50/50 contribution of wave and lift-induced drag increases. Moreover, the ONERA computation carried out for the as-tested shape with a laminar zone up to 10% chord has given a drag value of 247.7 counts. As the experimental drag evaluation from NTF is close to 248 counts, the numerical drag prediction of ONERA and the drag measurement of NASA are now in almost perfect agreement.

Acknowledgments

The author would like to thank D. Destarac and S. Esquieu, who developed the far-field drag extraction software used in this study following a theory elaborated by J. van der Vooren. The author also thanks his colleagues Mickaël Méheut for the grid deformation process and Ludovic Wiart for his constant help.

References

[1.] Hue, D., "Computational Drag and Moment Prediction of the NASA-CRM Configuration using the elsA Software and the Far-Field Approach in the framework of the 5th Drag Prediction Workshop," *AIAA Applied Aerodynamics Conference*, New Orleans, LA, June 2012, http://aaac.larc.nasa.gov/tsab/cfdlarc/aiaa-dpw/.

[2.] Rivers, M. B., Hunter, C. A., and Campbell, R., L., "Further Investigation of the Support System Effects and Wing Twist on the NASA Common Research Model," AIAA Paper 2012-3209, 2012.

[3.] Vassberg, J. C., DeHann, M. A., Rivers, S. M., and Wahls, R. A., "Development of a Common Research Model for Applied CFD Validation Studies," AIAA Paper 2008-6919, 2008.

[4.] Vassberg, J. C., "A Unified Baseline Grid about the Common Research Model Wing-Body for the Fifth AIAA CFD Drag Prediction Workshop," AIAA Paper 2011-3508, 2011.

[5.] Hue, D., "5th Drag Prediction Workshop: CFD studies using the elsA Solver and Far-Field Analyses," *Journal of Aircraft, Drag Prediction Workshop Special Section*, to be published in 2013/2014.

[6.] Cambier, L., and Gazaix, M., "elsA: An Efficient Object-Oriented Solution to CFD Complexity," AIAA Paper 2002-0108, Reno, 2002.

[7.] Gazaix, M., Jolles, A., and Lazareff, M., "The elsA Object-Oriented Computational Tool for Industrial Applications," *ICAS Congress*, 2002.

[8.] Destarac, D., "Far-Field / Near-Field Drag Balance Applications of Drag Extraction in CFD," *CFD-Based Aircraft Drag Prediction and Reduction,* VKI Lecture Series 2003-02, von Karman Institute for Fluid Dynamics, Rhode-Saint-Genèse, Belgium, 3-7 November 2003.

[9.] Van der Vooren, J., and Destarac, D., "Drag / Thrust Analysis of Jet-propelled Transonic Transport Aircraft; Definition of Physical Drag Components," *Aerospace Science and Technology,* Vol.8, No. 6, Sept. 2004, pp. 545-556.

[10.] Esquieu, S., "Reliable Drag Extraction from Numerical Solutions: Elimination of Spurious Drag," AVT Symposium, RTO-MP-AVT-147, Athens, Greece, 3-6 December 2007, Paper 42.

[11.] Destarac, D., "Drag Extraction from Numerical Solutions to the Equations of Fluid Dynamics: the Far-field Philosophy," *43eme Colloque d'Aérodynamique Appliquée de l'Association Aéronautique Astronautique de France*, Poitiers, 10-12 March 2008.

[12.] Hue, D., and Esquieu, S., "Computational Drag Prediction of the DPW4 Configuration Using the Far-Field Approach," *Journal of Aircraft*, Vol. 48, No. 5, Sept.-Oct. 2011, pp. 1658-1670.

[13.] Rivers, M. B., and Dittberner, A. "Experimental Investigation of the NASA Common Research Model," AIAA Paper 2010-4218, 2010.

[14.] Rivers, M. B., and Dittberner, A., "Experimental Investigations of the NASA Common Research Model in the NASA Langley National Transonic Facility and NASA Ames 11-Ft Transonic Wind Tunnel," AIAA Paper 2011-1126, 2011.

[15.] Zilliac, G., Pulliam, T., Rivers, M., Zerr, J., Delgado, M., Halcomb, N., and Lee, H., "A comparison of the Measured and Computed Skin Friction Distribution on the Common Resarch Model," AIAA Paper 2011-1129, 2011.

[16.] NASA, Langley Research Center, "Common Research Model," http://commonresearchmodel.larc.nasa.gov/.